

Research paper

Analysis of the metrics and mechanism of powder spreadability in powder-based additive manufacturing

Rui Xu^a, Wenguang Nan^{a,b,*}^a School of Mechanical and Power Engineering, Nanjing Tech University, Nanjing 211816, China^b Faculty of Engineering and Physical Sciences, University of Leeds, Leeds LS2 9JT, UK

ARTICLE INFO

Keywords:
 Additive manufacturing
 Powder spreading
 Powder spreadability
 DEM
 Jamming

ABSTRACT

Powder spreadability is critical to particle spread layer and thus the quality of final product in powder-based additive manufacturing, but the metrics and the underlying mechanics have not yet been well acknowledged. In this work, the metrics of spreadability are examined for powder with different size classes, and the factors affecting powder spreadability are analysed, in which both the cohesion and interlocking of particles are included. The simulation results are validated by comparing the total particle volume of spread layer against the experimental and numerical data in previous work. The results show that relative powder spreadability should be compared at the same ratio of the gap height to particle size, especially for the powders with different particle size classes. Powder spreadability is mainly controlled by the shear action of the blade on the heap, the stagnation effect due to rough surface of substrate, particle jamming around the gap region, and the effect of powder flowability on the movement of particles within the heap. Jamming makes powder spreadability different from powder flowability. As particle jamming is more prone for the particles with strong interlocking, powder spreadability is more sensitive to the rolling friction than the cohesion of particles, especially for the substrate surface with small roughness, although the rheological behaviour of bulk particles is similar in front of the gap. A physical model is proposed to predict the maximum fraction of spread layer at the specified gap height.

1. Introduction

Additive manufacturing (AM) has attracted great attention in a wide range of industrial applications [1–4], such as aerospace, biology, medicine, architecture. In powder-based manufacturing methods, powder spread layer directly affects the interaction between the particles and the laser or binder, and thus plays a vital role in the quality of final product. However, powder used in additive manufacturing is usually fine and cohesive, even in irregular shape (such as sand powder), and the gap between the spreader and work surface is usually narrow, i.e. a few of particle diameters to achieve a thin powder layer. It poses great challenges for the spreading process, such as particle jamming around the gap, insufficient amount of powder on the work surface, and in some cases, the powder even could not be spread through the specified gap height. Therefore, an in-depth understanding of the spreadability of the cohesive and frictional powder flowing through a narrow gap is helpful for achieving better quality of spread layer, further development of this technology and introduction of new materials.

Various work has been done to explore the effects of powder

materials and operation conditions on the spreading process through the experiments [5–8] and numerical simulation using discrete element method (DEM) [9–16]. However, the metrics and underlying mechanism of spreadability have not been thoroughly acknowledged [17]. The detailed definition of spreadability is firstly proposed by Nan et al. [18] and Ghadiri et al. [19], which is given as the ability of the powder to be spread uniformly as a thin layer of a few multiples of particle size without the formation of any empty patches, presence of agglomerates and rough surfaces. They also supposed that spreadability and flowability/fluidity are two different measures of the characteristics of powder flow, although they maybe inter-related. Snow et al. [20] attempted to establish the metrics of spreadability by comparing the powder coverage percentage of substrate, the rate of powder deposition, the average avalanching angle of the powder heap, and the rate of change of the avalanching angle. Ahmed et al. [21] proposed a simple method to access the spreadability, which was described as size and frequency of empty patches. They provided the detail of each step in their test procedure, and compared the results with the work of Nan et al. [18]. Le et al. [22] proposed a new method to examine powder

* Corresponding author at: School of Mechanical and Power Engineering, Nanjing Tech University, Nanjing 211816, China.

E-mail address: nanwg@njtech.edu.cn (W. Nan).

spreadability based on the high-precision morphology of spread layer using scanner technology, and showed that the quality of spread layer was a function of powder conditions and recoating strategies. Mussatto et al. [23] analysed the effects of powder morphology and spreading parameters on the spreadability, which was described by profile of the height and profile of the void volume measured from powder bed topography. However, no criterion was proposed to compare the relative spreadability of different powder. Nan et al. [24] clarified that excellent spreadability could only be obtained in a specified range of flowability, where the powder should be neither extremely cohesive nor excessively free-flowing with little frictional resistance. They also proposed the concept of dynamic spreadability, considering the demand of a high manufacturing rate in AM. Shaheen et al. [25] analysed the influence of particle material and process parameters on the spreadability, and showed that irregular particles, rough particle surfaces and high interfacial cohesion usually (but not always) lead to poor spreadability.

Following our previous work [18,19,21,24,26], the spreadability of powder used in powder-based additive manufacturing is detailed investigated. In Section 3, the metrics of powder spreadability are developed and examined for powder with different size classes. In Section 4, the factors affecting powder spreadability are explored with the analysis of underlying mechanism, and the difference between powder spreadability and flowability is highlighted, in which both particle cohesion and particle interlocking are included. In Section 5, the spreadability is further analysed, such as particle jamming, the effect of base roughness, and the comparison against the experimental and numerical data in previous work. A mathematical and physical model is also provided to predict the maximum fraction of spread layer at the specified gap height. This provides a further step towards better understanding of powder spreadability and jamming in additive manufacturing.

2. Methods

The simulation system consists of a spreading blade and a base, as shown in Fig. 1, where clumped cylinders are used to artificially describe the rough surface of the base in the real spreading process. The particles used in this work are gas-atomised 316 L stainless steel powder (15–55 μm), with number-based D_{10} , D_{50} and D_{90} of 20 μm , 32 μm and 45 μm , respectively. Based on statistical analysis of 2500 randomly selected particles from a series of SEM images, the particles are classified into 4 size classes [18], i.e. 15–25 μm , 25–35 μm , 35–45 μm and 45–55 μm , and the corresponding number frequency is 29.6%, 40.8%, 23.9% and 5.7%, respectively, as shown in Fig. 2. The particles are firstly poured in front of the blade, forming a heap, and then the blade is lifted vertically to the specified position, forming a gap with height of δ between the bottom of blade and the top tip of rough base. Afterwards, the blade accelerates

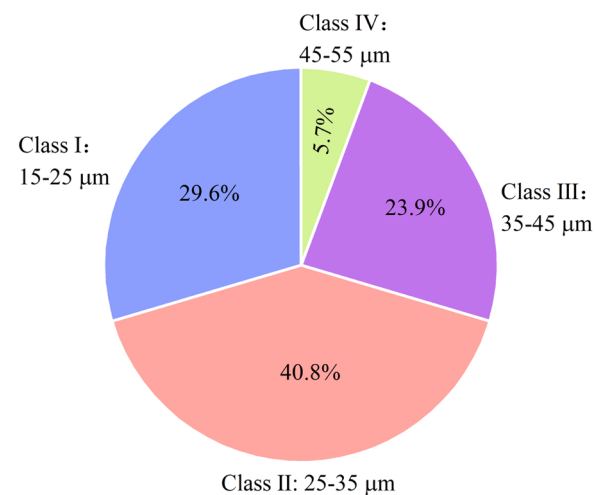


Fig. 2. Size distribution of particles characterised by the statistical analysis of 2500 randomly selected particles from a series of SEM images.

quickly in the spreading direction to the specified speed (i.e. $U=80 \text{ mm/s}$), and then moves forward at this constant speed, while the particles are spread onto the rough base by the blade, forming a spread layer with a length about 14.6 mm. The simulation system is periodic in the Y direction with a width of $W=10D_{90}$. The 12 mm spread layer and corresponding spreading process is used for analysis if not specified.

To describe the dynamics of particle flow in the spreading process, the particles are modelled as discrete entities and their motions are tracked individually by solving Newton's laws of motion [27,28], for which the Altair EDEM™ software package is used. The non-spherical particles (as shown in the SEM images in Fig. 3) are described by clumped spheres. For each size class, 5–10 particles are randomly selected, and their shapes are generated by overlapping a number of spheres, with totally 24 kinds of particles being used in the DEM simulation, as shown in Fig. 3. The physical and mechanical properties of a single particle involved in the simulation are all experimentally characterised by Nan et al. [18], which is summarised in Table 1, including friction coefficient using sliding test, interfacial surface energy using drop test. The materials of the blade and base are assumed to be the same as the particles shown in Table 1. For the interaction of particles, the normal contact force is described by Hertz model [27] with JKR theory [29]:

$$F_n = \frac{4E^*a^3}{3R^*} - \sqrt{8\pi G E^*a^3} \quad (1)$$

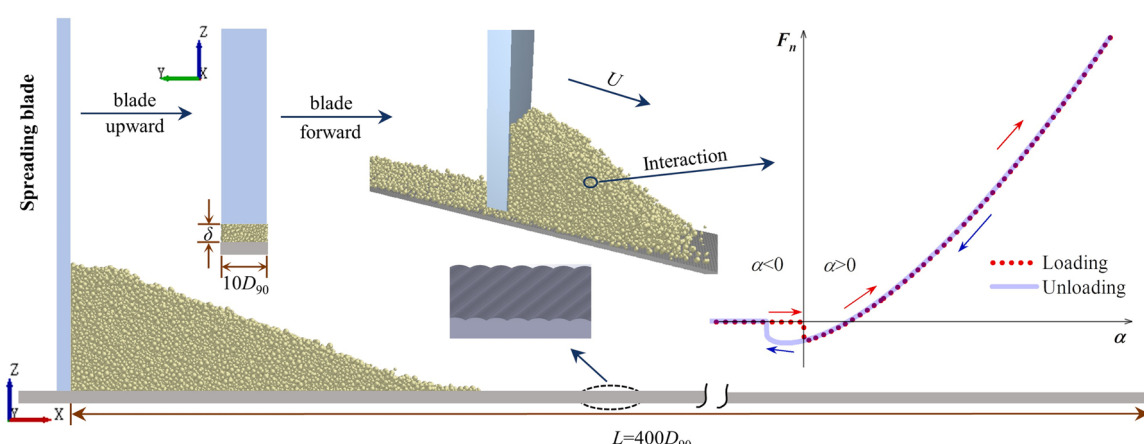


Fig. 1. Schematic of the spreading process of cohesive and frictional particles onto a rough base by a blade.

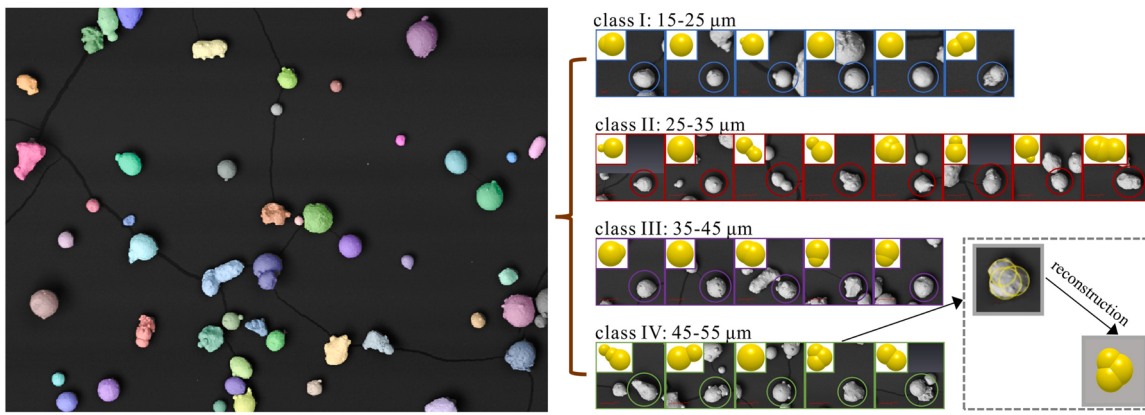


Fig. 3. Snapshots of SEM image of gas atomised steel powder (left) and totally 24 kinds of particles used in DEM simulation (right).

Table 1
Physical properties of single particle in the standard case, which is characterised by the experiment [18].

Parameter	Value
Diameter, D_{90} (mm)	0.045
Density, ρ (kg/m ³)	7980
Young's modulus, E^* (GPa)	211
Friction coefficient, μ	0.5
Restitution coefficient, e	0.64
Surface energy, Γ (mJ/m ²)	9

* * In the DEM simulation, Young's modulus is scaled down to 2.1 GPa, and surface energy is correspondingly scaled down to 1.4 mJ/m².

where Γ is the interfacial surface energy; E^* is the equivalent Young's modulus; a is the contact radius, which could be calculated from physically normal overlap α . To speed up the simulation, Young's modulus is scaled down to 2.1 GPa while the interfacial surface energy is adjusted to 1.4 mJ/m² according to following law:

$$\frac{\Gamma_{DEM}}{\Gamma_{exp}} = \left(\frac{E_{DEM}}{E_{exp}} \right)^{2/5} \quad (2)$$

3. Metrics of spreadability

When the spreading process is finished, a thin layer of particles will be formed on the rough base. Based on previous work in Nan et al. [18, 24] and Ghadiri et al. [19], the spreadability of powder used in powder spreading process of AM is defined as the ability of the powder to be spread evenly through a narrow gap (i.e. a few times of D_{90}), forming a thin and dense layer without any defects such as particle clusters, empty patches, particle segregation. Good spreadability usually indicates that the particle spread layer is dense and uniform (i.e. particle size distribution is unchanged along the spreading direction), and there are no empty patches. Based on this concept, three kinds of metrics are introduced in this work to quantitatively characterise powder spreadability: empty patches, particle volume of spread layer, and particle segregation within spread layer.

a) Empty patches. Empty patches are referred to the area of base not covered by particles' projections. The snapshots of the spread layer with high resolution are obtained after spreading, and the total area of empty patches is calculated by ImageJ software.

b) Particle volume of spread layer. The total volume of particles within the spread layer is calculated and normalised as:

$$\phi = \frac{M_p}{\rho LW} \quad (3)$$

where M_p is the total mass of particles within the spread layer; ρ is the density of an individual particle; L and W are the length and width of spread layer, respectively.

c) Powder segregation. Size distribution of the particles within the spread layer is analysed, and it is compared with the bulk powder before spreading. Meanwhile, the spread layer is divided into four identical cells along the spreading direction, and the local segregation index is calculated based on the frequency of each size class of particles:

$$SI_j = \frac{\sigma_j}{x_{j0}} \quad (4)$$

$$\sigma_j^2 = \sum_{i=1}^N \frac{w_i(x_{ji} - x_{j0})^2}{\sum_{i=1}^N w_i} \quad (5)$$

where $i = 1-N$ refers to the index of cell used for analysis; $N = 4$ is the number of cells; $j = 1-4$ refers to the index of powder size class (as shown in Fig. 2); x_{ji} and x_{j0} are the frequency of particle size class j in the spread layer after spreading and the initial particle bed before spreading, respectively; w_i is the total volume of all particles in cell i . If the segregation index SI_j is equal to 0, the frequency of particle size class j is identical to that of the initial particle bed in each cell. Here, the PSD of initial particle bed is referred to Fig. 2, i.e. $x_{j0} = 29.6\%, 40.8\%, 23.9\%, 5.7\%$, respectively.

To further illustrate the metrics of powder spreadability, three kinds of powder with different value of D_{90} are used here, i.e. $D_{90} = 67.5 \mu\text{m}$, $45 \mu\text{m}$ and $22.5 \mu\text{m}$. Each metric of spreadability is analysed for these powders at three gap heights, i.e. $50 \mu\text{m}$, $100 \mu\text{m}$ and $150 \mu\text{m}$, as shown in Sections 3.1–3.3. For $D_{90} = 45 \mu\text{m}$, it is the standard case, with other physical properties described in Section 2. For $D_{90} = 67.5 \mu\text{m}$ and $22.5 \mu\text{m}$, the size of all 24 kinds of particles (shown in Fig. 3) is scaled with the ratio of 1.5 and 0.5, respectively, while other physical properties are the same as the case with $D_{90} = 45 \mu\text{m}$. For convenience, the powder with $D_{90} = 67.5 \mu\text{m}$, $45 \mu\text{m}$ and $22.5 \mu\text{m}$ is assigned as powder A, powder B and powder C, respectively. The powder heap before spreading is shown in Fig. 4. With the decrease of D_{90} , the powder heap becomes more slope, thus, the flowability of bulk powder is reduced. This is intuitively expected, as the Bond number increases with the decreases of particle size:

$$Bo = \frac{F_c}{m_0 g} = \frac{9}{2} \frac{\Gamma}{\rho g D_{90}^2} \quad (6)$$

where $F_c = 3\pi\Gamma D_{90}/4$ is the maximum pull-off force in JKR theory; m_0 is the mass of an individual particle with diameter of D_{90} .

3.1. Empty patches

Fig. 4 shows the snapshots of final spread layer after spreading. For

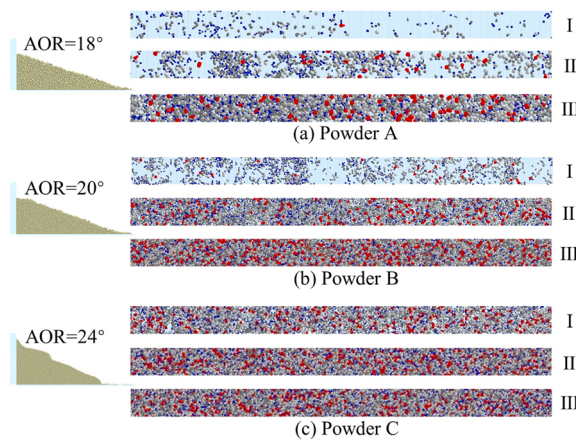


Fig. 4. Snapshots of the powder heap before spreading and the spread layer after spreading at different gap heights (I: $\delta = 50 \mu\text{m}$, II: $\delta = 100 \mu\text{m}$, III: $\delta = 150 \mu\text{m}$).

powder A at small gap height, many empty patches with different sizes are formed in the spreading direction. The empty patches are due to the transient jamming around the blade [18], the obvious evidence of which is discussed in Section 5. For powder A at the gap height of $50 \mu\text{m}$, almost no particles could be spread onto the base, and about 88% surface of the base is occupied by empty patches, as shown in Fig. 5(a). As

shown in Fig. 4(a), with the increase of gap height, the occurrence of jamming is reduced, and thus the particle spread layer becomes more uniform with fewer patches and more large particles. Correspondingly, the area percentage of empty patches decreases sharply. For example, as the gap height increases from $50 \mu\text{m}$ to $150 \mu\text{m}$, the area percentage of empty patches decreases from 88% to 10%.

Compared to powder A, empty patches are much less prone for powder B and C at the same gap height, as shown in Fig. 5(a) and Fig. 4. For example, at the gap height of $100 \mu\text{m}$, the area percentage is about 50% for powder A, but it is only 0.5% for powder C. However, it does not suggest that the probability of forming empty patches is powder A > powder B > powder C. The probability of producing empty patches should be more related to the relative ratio of gap height to particle size D_{90} , which could be concluded from Fig. 5(b). It shows that the area percentage of empty patches decreases greatly with the increase of δ/D_{90} for all kinds of particles. It also indicates that the probability of forming empty patches or spreadability is not directly related to Bond number or flowability.

3.2. Particle volume of spread layer

Fig. 6 shows the normalised total volume of particles within the spread layer. As shown in Fig. 6(a), at the same gap height, total particle volume of spread layer for powder C is much larger than that for powder A and B, indicating a denser spread layer for the powder with smaller D_{90} . With the increase of gap height, the total volume of particles within spread layer increases almost linearly. This is because that the shear

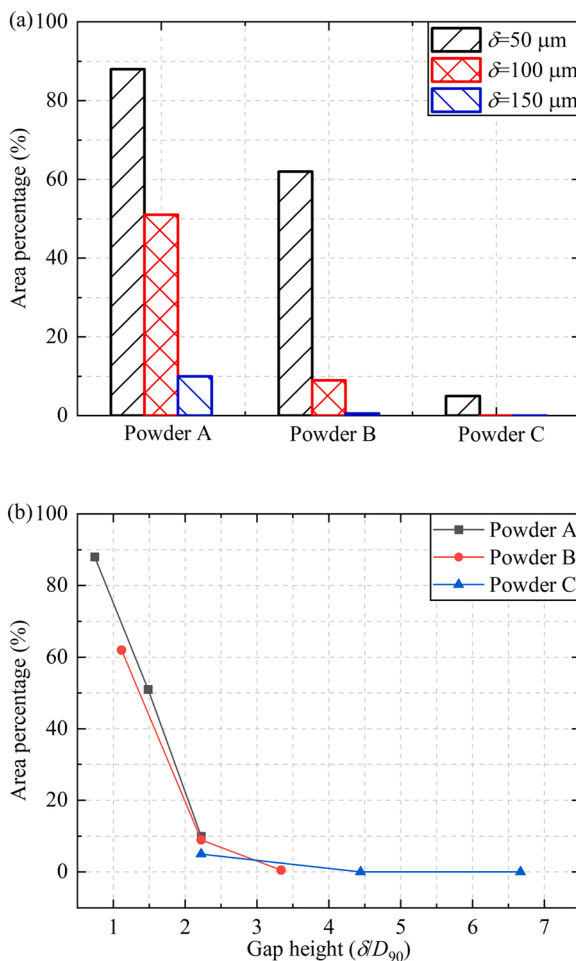


Fig. 5. Area percentage of empty patches within the spread layer at different gap heights for powder A ($D_{90} = 67.5 \mu\text{m}$), powder B ($D_{90} = 45 \mu\text{m}$) and powder C ($D_{90} = 22.5 \mu\text{m}$).

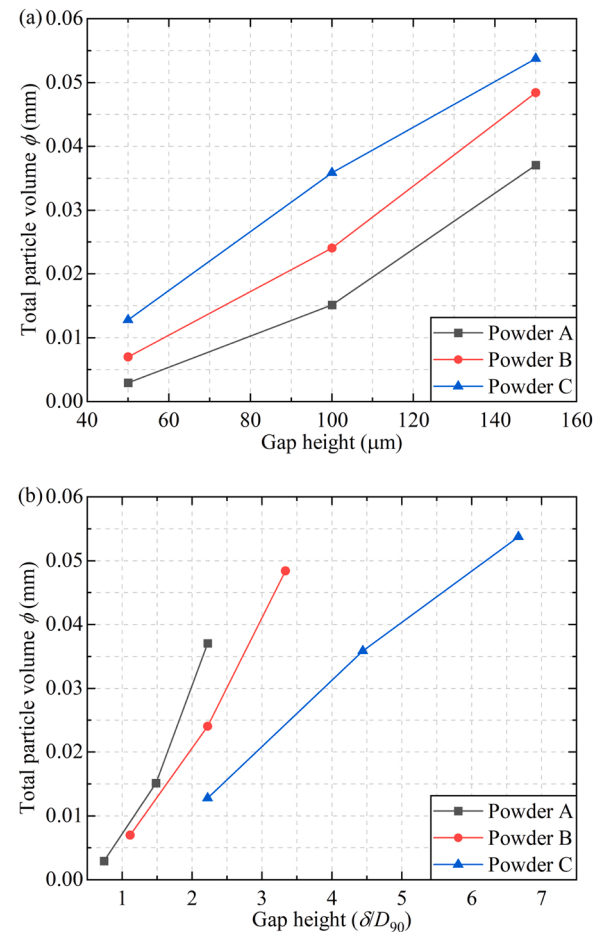


Fig. 6. Total particle volume ϕ of the spread layer at different gap heights for powder A ($D_{90} = 67.5 \mu\text{m}$), powder B ($D_{90} = 45 \mu\text{m}$) and powder C ($D_{90} = 22.5 \mu\text{m}$), where $\phi = \sum m_p / (\rho_p L W)$.

band could be better developed [30], thus, the shear strength on the heap by the blade is enhanced, resulting in more particles detaching from the heap and deposited on the base. Therefore, the higher the gap height or the smaller of the particle size, the more particles within the spread layer. However, it does not suggest that the ability of producing dense particle spread layer is powder A < powder B < powder C. The denser spread layer in powder C is due to the size effect rather than better spreadability. Here, the total volume of particle spread layer is further plotted against δ/D_{90} , as shown in Fig. 6(b). It shows that at the same ratio δ/D_{90} , the total volume of particle spread layer is powder A > powder B > powder C, indicating that the spreadability is powder A > powder B > powder C. Therefore, the ability of producing dense spread layer should be compared at the same ratio of gap height to particle size, instead of absolute value of gap height.

3.3. Powder segregation

Fig. 7 shows the particle size distribution of the spread layer and the segregation index of each particle size class of powder. For powder A, at the gap height of 50 μm , there are almost no particles of classes III and IV on the spread layer, while the number frequency of particles of class I is much larger than the value of initial particle bed. It indicates that under narrow gap height, there are more small particles and fewer large particles on the base, which is consistent with the snapshot of spread layer in Fig. 4. Compared to powder A, for the spread layer of powder B and C, the number frequency of particles of all size classes deviates less from

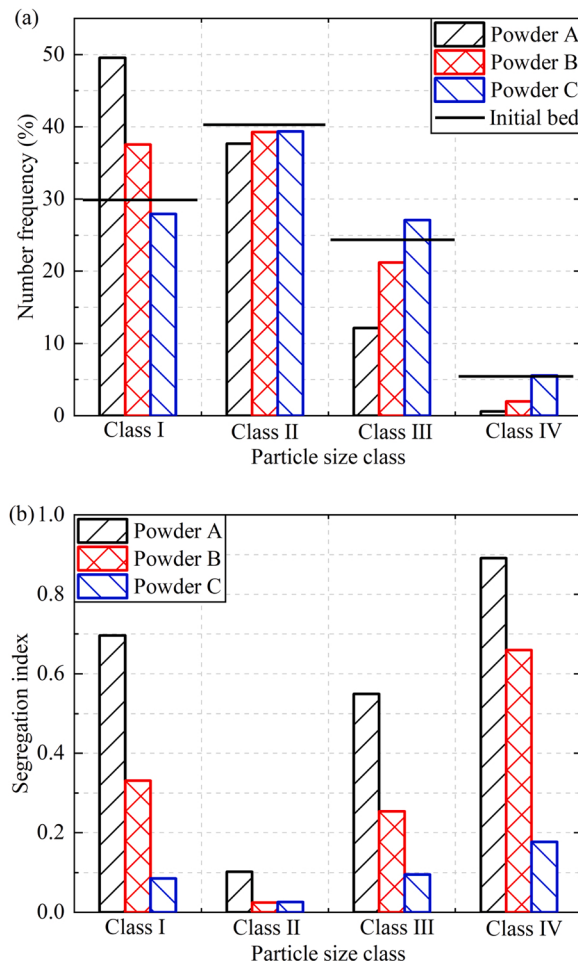


Fig. 7. Particle number frequency (a) and segregation index (b) of the spread layer at the gap height of 50 μm for powder A ($D_{90} = 67.5 \mu\text{m}$), powder B ($D_{90} = 45 \mu\text{m}$) and powder C ($D_{90} = 22.5 \mu\text{m}$).

that of initial particle bed, especially for powder C. This shows that the higher the gap height or the smaller the particle size, the more uniform of particle spread layer. Correspondingly, as shown in Fig. 7(b), for all kinds of powder, the segregation index of size class IV is the largest, which indicates that large particles are easier to segregate. This is expected as jamming at the gap region is more prone for large particles. With the decrease of D_{90} , the segregation index for each size class decreases.

Fig. 8 shows the average segregation index SI of all particles size classes, which is plotted against the relative ratio of gap height δ to particle size D_{90} . It shows that the average segregation index decreases in an exponential form with the increase of δ/D_{90} . Thus, the segregation index is affected by both the particle size D_{90} and gap height at the same time, and the ratio of gap height to particle size should be involved when comparing the relative spreadability of different kinds of powder.

4. Factors affecting spreadability

Spreadability is affected by various factors, especially particle properties. Here, the effects of interfacial surface energy and rolling friction coefficient as well as particle shape on powder spreadability are investigated, as shown in Table 2. In the standard case, as described in Section 2, interfacial surface energy is 1.4 mJ/m², and the rolling friction coefficient is 0.001. For the case varying interfacial surface energy, as shown in case I in Table 2, five kinds of value is used, i.e. 0 mJ/m², 1.4 mJ/m², 5.2 mJ/m², 9 mJ/m², 11.2 mJ/m². Meanwhile, rolling friction coefficient remains constant at 0.001, and non-spherical particles are used. Here, cohesion number is used to describe the effect of interfacial surface energy:

$$Coh = \frac{\Gamma^{5/3}}{\rho g E^{*2/3} R^{*8/3}} \quad (7)$$

where E^* is the equivalent Young's modulus; $R^* = D_{90}/4$ is the equivalent radius between two identical particles with diameter of D_{90} . Correspondingly, the cohesion number is 0, 0.003, 0.03, 0.07, 0.1, respectively. For the case varying particle shape, as shown in case II in Table 2, all 24 kinds of particles in Fig. 3 are artificially simplified as spherical shape without changing the volume. Meanwhile, two cohesion number is used, i.e. 0.003 and 0.07, and rolling friction coefficient remains constant at 0.001. For the cases varying rolling coefficient, as shown in case III in Table 2, four kinds of value is used, i.e. 0.001, 0.01, 0.1, 0.4, where all particles are in spherical shape and cohesion number remains constant at 0.003. For all cases in this section, the gap height is

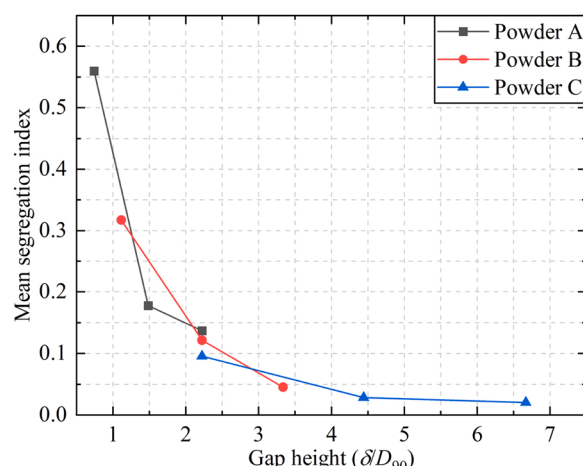


Fig. 8. Variation of mean segregation index SI of the spread layer with the gap height normalized by D_{90} for powder A ($D_{90} = 67.5 \mu\text{m}$), powder B ($D_{90} = 45 \mu\text{m}$) and powder C ($D_{90} = 22.5 \mu\text{m}$), where SI is the average value of segregation index SI_j of four particle size classes.

Table 2

Range of particle properties in different cases.

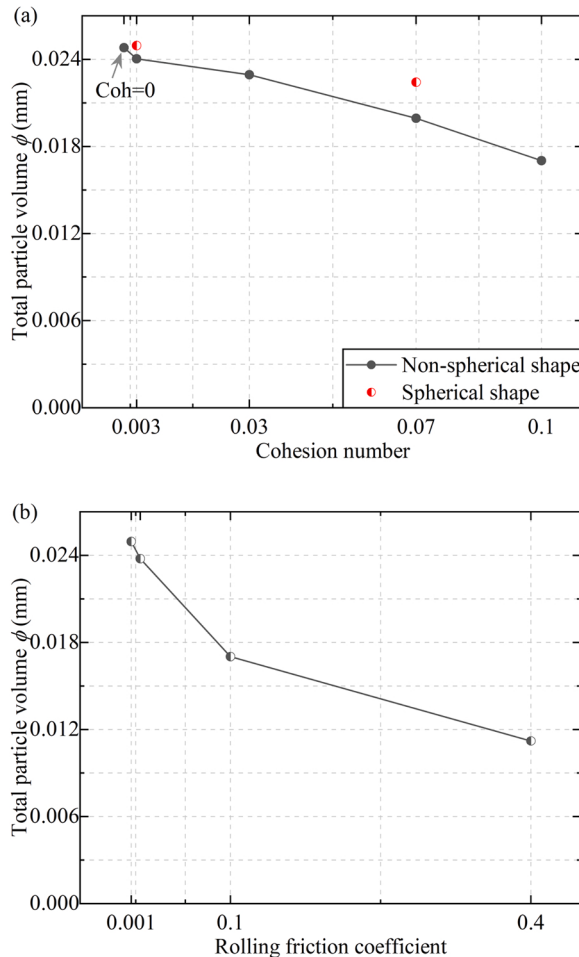
	Cohesion number	Particle shape	Rolling friction
Case I	0–0.1	non-spherical ^a	0.001
Case II	0.003/0.07	spherical ^a	0.001
Case III	0.003	spherical ^a	0.001–0.4

^a non-spherical shape: total 24 kinds of particles are characterised from experiment, spherical shape: each particle is artificially simplified as spheres while keeping volume unchanged.

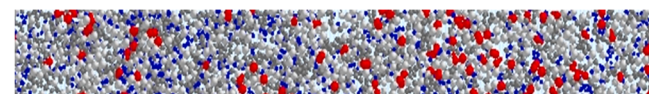
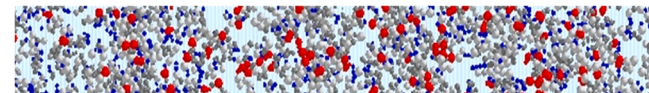
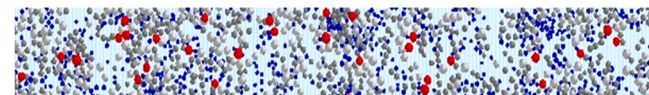
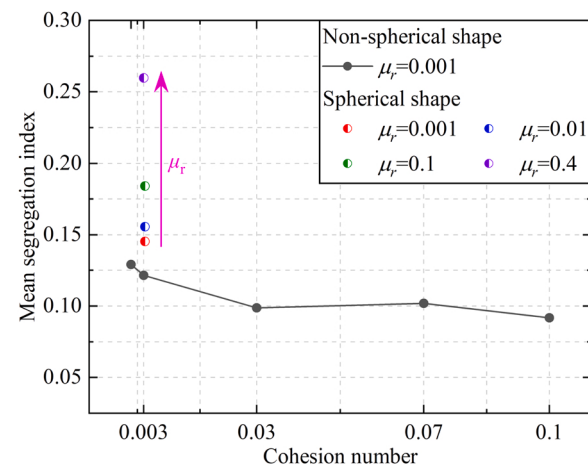
100 μm , $D_{90} = 45 \mu\text{m}$. For other properties, the value is the same as the standard case described in [Section 2](#), if not specified.

[Fig. 9](#) shows the variation of total particle volume of spread layer with cohesion number and rolling friction coefficient. As shown in [Fig. 9](#) (a), with the increase of cohesion number, the total particle volume decrease, i.e. the spreadability becomes worse. It is also clear that when changing the particles from non-spherical to spherical shapes, there is a slight increase for total particle volume. As shown in [Fig. 9](#)(b), with the increase of rolling friction, the total volume shows a sharp decrease, i.e. the spreadability is significantly reduced. And the extent of decrease is larger than the ones with increasing cohesion number, indicating that spreadability is more sensitive to the rolling friction of particles.

[Fig. 10](#) shows the snapshots of spread layer after spreading. Compared to the standard case ([Fig. 10\(a\)](#)), more and larger empty patches could be found in other two cases, especially for the case with $\mu_r = 0.4$, in which only a few of large particles could be found in the spread layer. Correspondingly, the mean segregation index SI is shown in



[Fig. 9](#). Variation of total particle volume of the spread layer with cohesion number and rolling friction coefficient of particles at the gap height of 100 μm .

(a) Non-spherical shape from experiment, Coh=0.003, $\mu_r=0.001$ (b) Non-spherical shape from experiment, Coh=0.1, $\mu_r=0.001$ (c) All particles in spherical shape, Coh=0.003, $\mu_r=0.4$ [Fig. 10](#). Snapshots of particle spread layer at the gap height of 100 μm .

[Fig. 11](#). Mean segregation index of the spread layer at the gap height of 100 μm : non-spherical shape with $\mu_r = 0.001$ and different interfacial surface energy (solid symbols), spherical shape with different μ_r and Coh= 0.003 (semi-open symbols).

[Fig. 11](#). With the increase of cohesion number, the segregation index decreases slightly. With the increase of rolling friction, the segregation index shows a sharp increase, resulting in significant decrease of spreadability, especially at large rolling friction. It suggests that the segregation index is more sensitive to the rolling friction, which is similar to that of the total particle volume of spread layer.

It should be noted that the mechanisms of the variation of powder spreadability due to cohesion number and rolling friction are different, which could be depicted from the force analysis and particle trajectories shown below. [Fig. 12](#) shows the time-averaged and non-dimensional downward force on the base ($F_{z,\text{base}}/Mg$) and shear traction (μ_{blade} on the blade and μ_{base} on the base). The shear traction is given as:

$$\mu_{\text{blade}} = \frac{F_{x,\text{blade}}}{Mg} \quad (8)$$

$$\mu_{\text{base}} = \frac{F_{x,\text{base}}}{F_{z,\text{base}}} \quad (9)$$

where $F_{x,\text{blade}}$ is the force on the blade in the spreading direction; Mg the transiently total weight of heap in front of the blade; $F_{x,\text{base}}$ and $F_{z,\text{base}}$ are the force on the base in the spreading direction and downward direction, respectively.

As shown in [Fig. 12\(a\)](#), with the increase of cohesion number, the downward force on the base decreases, and the extent of decrease is

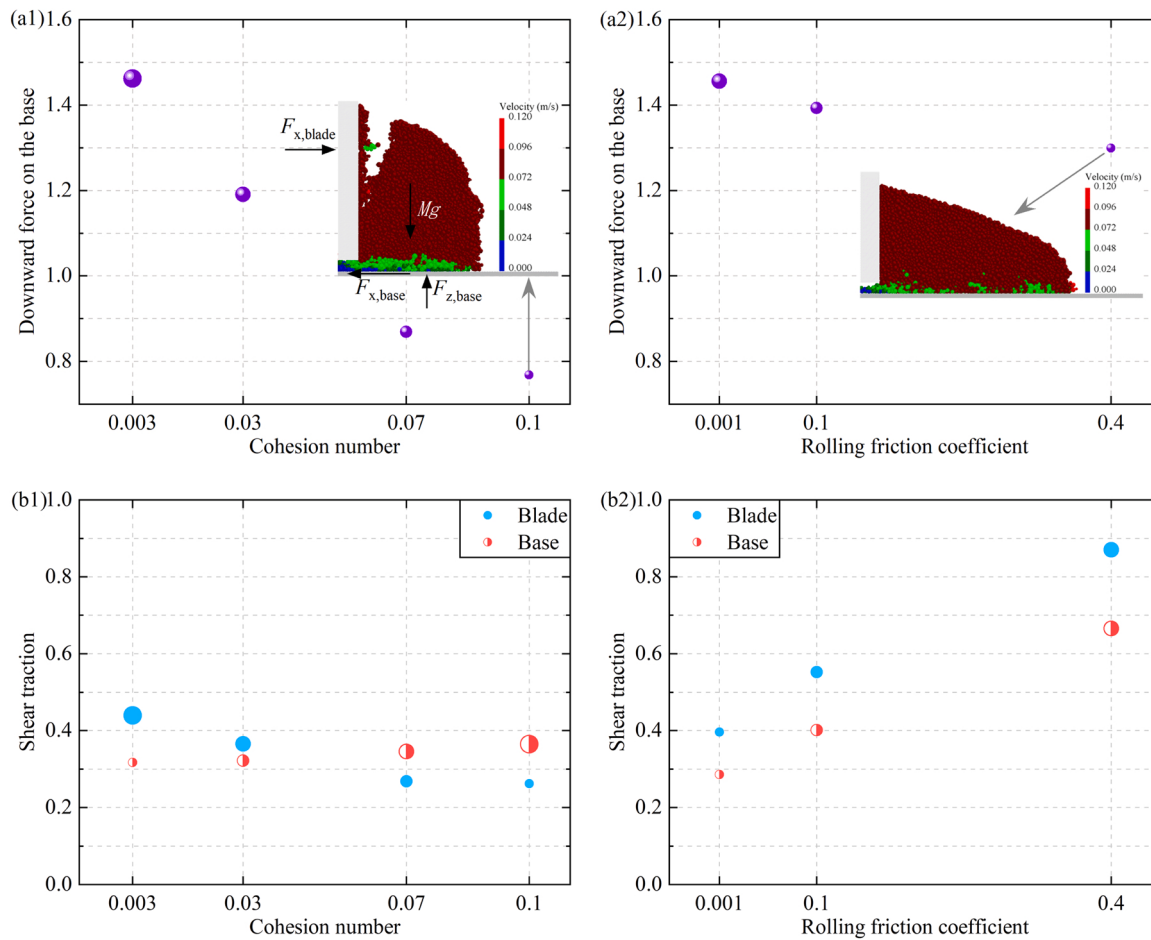


Fig. 12. Variation of blade/base-heap interaction with cohesion number and rolling friction: (a1) & (a2)-downward force on the base ($F_{z,\text{base}}/Mg$); (b1) & (b2)-shear traction on the blade ($F_{x,\text{blade}}/Mg$) and base ($F_{x,\text{base}}/F_{z,\text{base}}$).

much larger than that of rolling friction. This is mainly due to that the heap does not contact well with the blade and base at large cohesion number, as shown in the subgraph in Fig. 12(a). For example, for the cases with $\text{Coh}=0.07$ and 0.1 , the downward force on the base is even less than the total weight of the heap. As shown in Fig. 12(b), with the increase of cohesion number, the blade force in the spreading direction $F_{x,\text{blade}}$ decreases, which is mainly due to the reduction of the contact area between the heap and the blade. With the increase of rolling friction, the blade force $F_{x,\text{blade}}$ increases significantly, indicating that the shear action of the blade on the heap is enhanced. It also shows that the heap is more difficult to be sheared by the blade. Correspondingly, the shear friction of the heap on the base is more sensitive to the rolling friction, indicating that the stagnation effect is more enhanced in the case with large rolling friction. For example, compared to the standard case, i.e. $\mu_{\text{base}} \approx 0.3$, the shear friction between the heap and base only shows a slight increase when the cohesion number increases to 0.1 , but the increase could be significant (about 2 times) when the rolling friction increases to 0.4 . Therefore, for the case with large cohesion number, the heap tends to form agglomerates, and the heap does not contact well with the blade and base, weakening the blade shear action on the heap, while the stagnation effect of the base does not show much change. For the case with large rolling friction, both the shear action of the blade and the stagnation effect of the base on the heap are enhanced.

Fig. 13 shows the trajectories of particles, where the abscissa is the relative position of the particle centre x with respect to the blade centre x_{blade} . The particles, which end up in the box shown in the subgraph in Fig. 13(a), i.e. the region with a length of $2D_{90}$ in the final spread layer ($t = 0.2$ s), are selected as tracked particles, and their trajectories from

0.0 s to 0.2 s are analysed. More information of this method could be found in Nan et al. [31]. As shown in Fig. 13(a), for the standard case and the case with more cohesive particles ($\text{Coh}=0.1$), the averaged trajectory of tracked particles is similar, i.e. shifting downwards and then moving almost horizontally. For the case with $\mu_r = 0.4$, the averaged trajectory is in a very simple pattern, i.e. straight towards the behind of the blade ($x = 0$), and the vertical position of particles is much lower than that of other cases. It could be further illustrated from the trajectory of each particle, as shown in Fig. 13(b-d), where each curve corresponds to the route of an individual particle selected from the spread layer after spreading (i.e. coloured particles in the subgraph in Fig. 13(a)). In the standard case, as shown in Fig. 13(b), the trajectories of the tracked particles are like a hook: 1) as the particle bed is pushed by the blade, the tracked particles are moved to higher positions; 2) they then avalanche down within the heap or along the slope of the heap; 3) they reach the rough base with vertical position less than the gap height, and finally they are collected at the gap to form a thin layer. In the case with larger cohesion number, as shown in Fig. 13(c), the tracked particles move in a similar pattern, but the route is shorter. However, in the case with $\mu_r = 0.4$, the tracked particles move in a different pattern, and the particles forming the final layer are mainly from the lower part of the heap, as shown in Fig. 13(d). Therefore, with the increase of cohesion number and rolling friction, the motion of particles is weakened, especially the case with large rolling friction. It could be also found from the rheological behaviour of particles in front of the gap, i.e. a region with the size of $4D_{90} \times 10D_{90} \times 100 \mu\text{m}$, where the calculation details could be found in Appendix. As shown in Table 3, with the increase of cohesion number or rolling friction, the bulk friction increases, resulting in worse

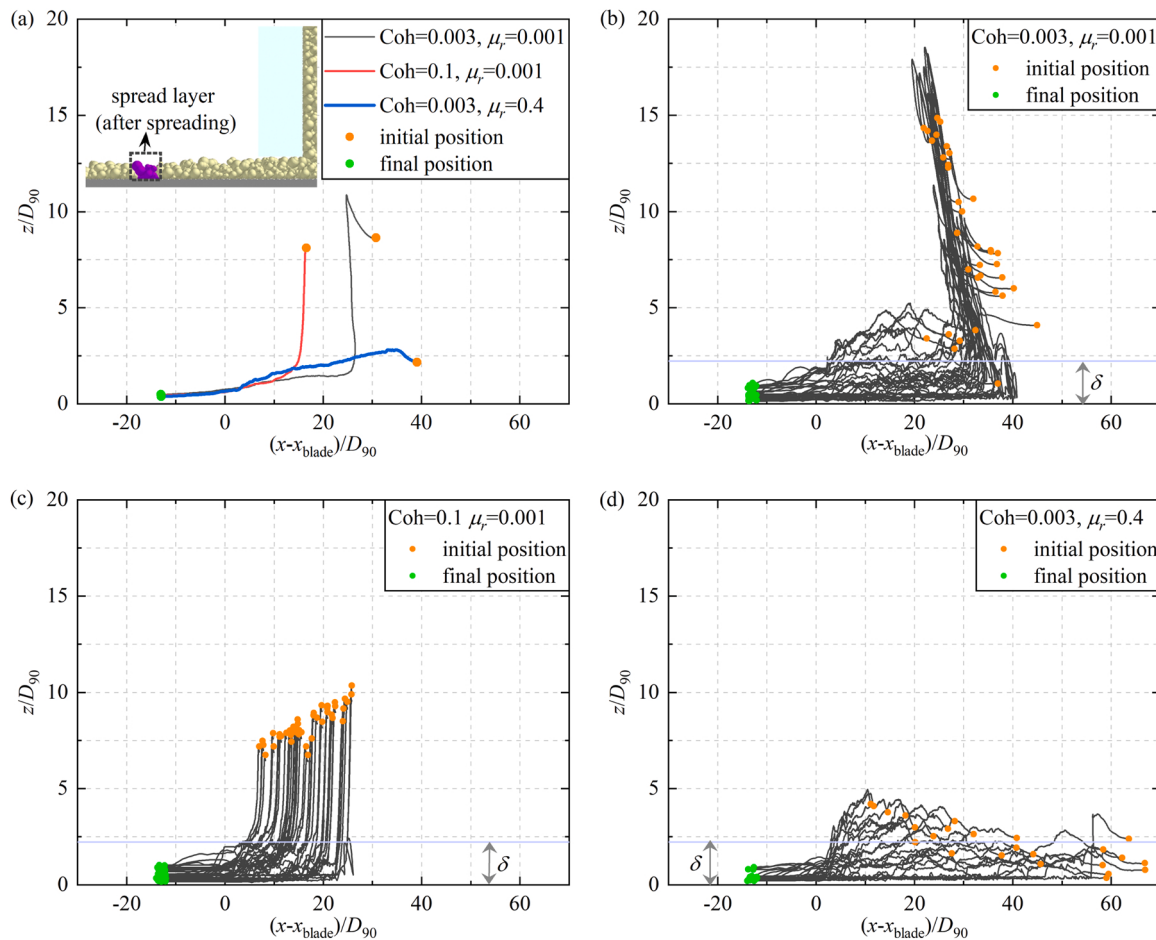


Fig. 13. Trajectories of particles forming the spread layer, where the abscissa is the relative position of the particle centre x with respect to the blade centre x_{blade} : (a) mean trajectories; (b-d) trajectory of each selected particle.

Table 3

Rheological behaviour of particles in front of the gap for the case with rough base.

Coh	μ_r	Normal stress (Pa)	Shear stress (Pa)	Bulk friction	Inertial number
0.003	0.001	18.1	22.1	1.22	0.76
0.07	0.001	12.7	19.8	1.56	0.90
0.003	0.4	17.1	27.7	1.62	0.78
0.1	0.001	12.8	19.8	1.55	0.90

flowability.

Therefore, the spreading process of particles could be summarised in Fig. 14: particles detach from the heap, they then enter the gap and deposit on the base, and during this process, the depletion region due to the detachment of particles is re-filled by the surrounding particles, which move in a route like a hook. The first stage is mainly controlled by the shear action of the blade and the stagnation effect of the base, and the second stage is significantly affected by the transient jamming near the gap, while the third stage is mainly affected by the effect of powder flowability on the movement of particles within the heap. With the increase of cohesion number, both the shear strength of blade on the heap and flowability are reduced while the stagnation effect of base on the heap does not change much, resulting in the decrease of spreadability. With the increase of rolling friction, although the shear strength and stagnation effect are both enhanced, the interlocking between particles is too strong to allow the circulation of particles within the heap, as shown in Fig. 13(d), slowing the re-filling process of particles.

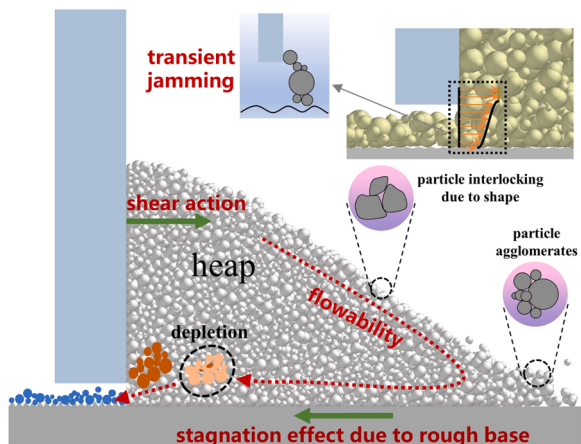


Fig. 14. Illustration of the spreading of particles from the heap onto the rough base at single-particle scale.

Meanwhile, the interlocking between particles significantly promotes the occurrence of transient jamming, as shown in Fig. 15, where several significant peaks of shear stress could be found, and the largest peak could even be hundred times of the time-averaged value. Under these combined effects, the spreadability is reduced, and the extent of decrease is larger than that of cohesion number.

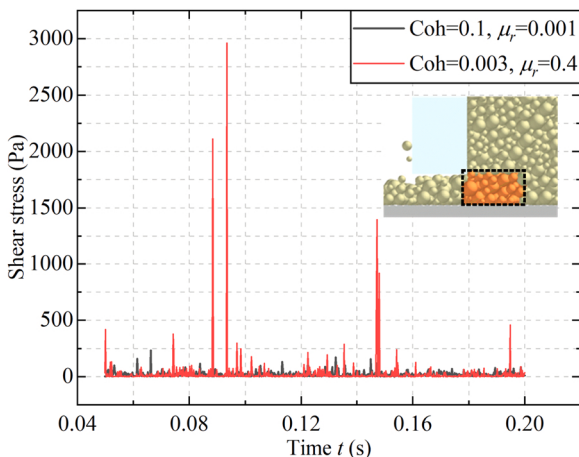


Fig. 15. Variation of shear stress of the particles in front of the gap with time.

5. Discussions

Compared to particle size, the clearance between the blade tip and base is very narrow, resulting in the occurrence of particle jamming [18]. Besides the peaks of shear stress shown in Fig. 15, another obvious evidence is burst-particles, following the collapse of jamming state. They are referred to the particles being busted into the sky, under the effect of the energy stored during the forming process of jamming, as shown in the subgraph in Fig. 16. It shows that the burst-particles usually fly through the gap in the opposite direction of the blade movement, and the particles are observed to be smaller than the gap height. Fig. 16 also shows the variation of the momentum of fly particles in the spreading direction (x direction) with time, where the cases with powder B and powder C are compared. Here, particle momentum p_x is normalised by that of an individual particle with the diameter of D_{90} and velocity of U :

$$p_x = \frac{\sum m u_x}{m_0 U} \quad (10)$$

where m is the mass of an individual particle; m_0 is the mass of a particle with diameter of D_{90} ; U is the blade speed. Here, only the particles with vertical position higher than $(\delta + D_{90})$ are considered. For powder C, the momentum is small but always positive, indicating that most particles are dragged forward by the blade. On the contrary, for powder B, several strong negative peaks are found, and the local position of the base underneath the burst particles is almost empty without particles. It also

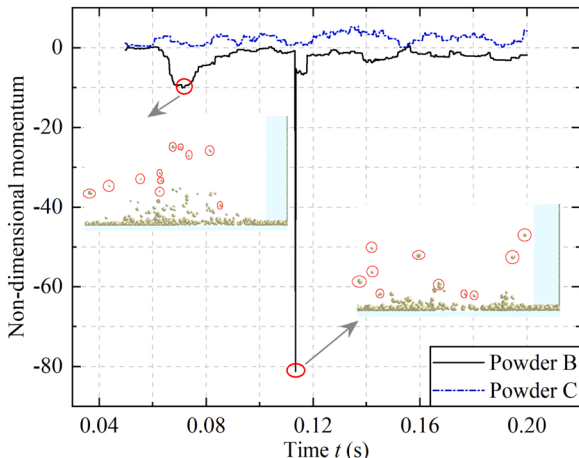


Fig. 16. Variation of total momentum (x direction) of burst particles with time at the gap height of $50 \mu\text{m}$ for powder B ($D_{90} = 45 \mu\text{m}$) and powder C ($D_{90} = 22.5 \mu\text{m}$).

shows that jamming are more prone for larger particles.

It should be noted that the spreadability of different kinds of powder should be examined at the same surface roughness of the base, especially for the particles with large rolling friction or irregular shape. Fig. 17 compares the total particle volume of spread layer for the cases using rough and smooth base, where the rough base is artificially made up of clumped cylinders, i.e. the same as the standard case shown in Fig. 1, and the smooth base is referred to the plane plate without any roughness. Compared to the case using rough base, the total particle volume of spread layer shows a decrease in the case using smooth base. It is interesting that for the case with $\mu_r = 0.4$, there are almost no particles spread onto the base, which is much different to the one shown in Fig. 10 (c). However, as shown in Table 3 and Table 4, as the surface of the base changes from rough to smooth, the rheological behaviour of the particles in front of the gap does not show much change, especially the bulk friction coefficient. Actually, it is more related to the stagnation effect of the base and the particle jamming around the gap region instead of the flowability of powder. The results also indicate that the roughness of the base should be large enough to retain the moving particles within the heap and break the jamming state of the particles. Otherwise, the whole heap is dragged forward by the blade, and the particles are jammed near the gap with very a long survival time, resulting in no particles detaching from the heap and being spread on the base, and thus a very bad spreadability. This could be further analysed from Fig. 18, where the shear stress of particles in front of the gap is illustrated. Compared to the case with $\mu_r = 0.001$, there is almost no fluctuation of the shear stress for the case with $\mu_r = 0.4$, which is contradictory to the nature of flow of discrete particles. It indicates that the particles in front of the gap almost move like a slug, and the jammed particles slide on the base without being interrupted by the shear action of blade and stagnation effect of the base. It agrees well with the subgraph in Fig. 18, where particles jamming in front of the gap could be clearly observed. In this case, the spreadability is dominated by particle jamming. It is also much different from the transient jamming occurred in other cases, where jamming disappears quickly and forms again, resulting in a very short survival time and high frequency of jamming events.

For the total particle volume of spread layer, it is the only metric of spreadability which could be easily measured in both experiment and simulation. Here, the data in this work is compared with the data re-calculated/directly from the literature, as shown in Fig. 19. As not all details were provided in the articles, only partial work is included here, i.e. experimental data in Nan et al. [24], and Zhang et al. [32], numerical data in Nan et al. [18], Si et al. [33], Xiang et al. [34], Wu et al. [9], Yao et al. [35] and Zhang et al. [32], in which the spreading speed is around 80 mm/s . Raw information involved in these data is shown in

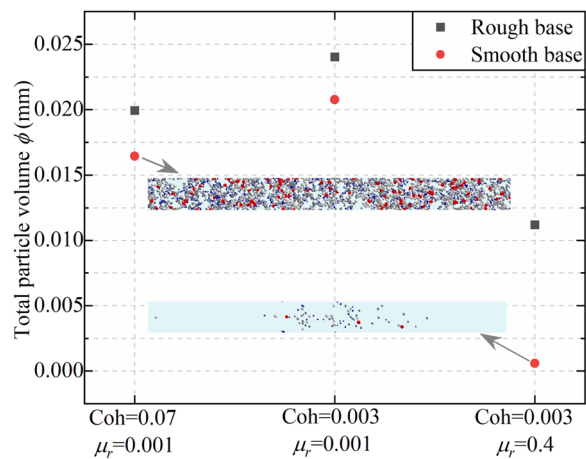


Fig. 17. Comparisons of total particle volume of the spread layer between the cases with rough and smooth base.

Table 4

Rheological behaviour of particles in front of the gap for the case with smooth base.

Coh	μ_r	Normal stress (Pa)	Shear stress (Pa)	Bulk friction	Inertial number
0.003	0.001	14.0	17.7	1.26	0.86
0.07	0.001	8.1	12.8	1.59	1.13
0.003	0.4	17.8	30.8	1.73	0.76

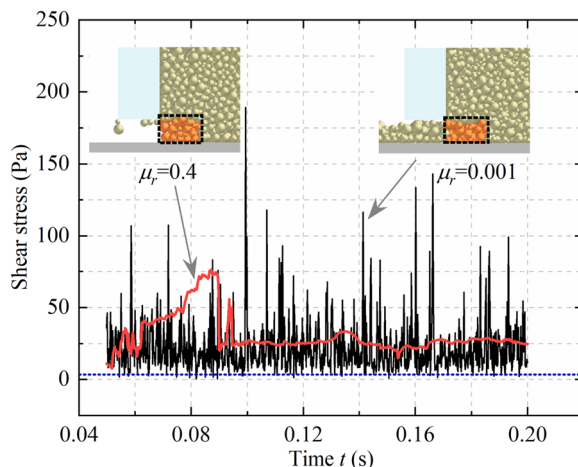


Fig. 18. Variation of shear stress of particles in front of the gap with time for the cases using smooth base.

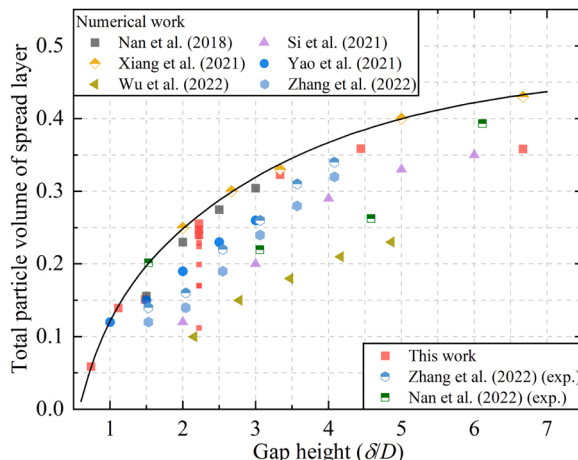


Fig. 19. Variation of total particle volume of the spread layer with gap height, where the total particle volume is normalised by $LW\delta$, and the gap height δ is normalised by particle diameter D , where D =number-based D_{90} in this work and Nan et al. [18,24]; D =volume-based D_{50} in Xiang et al. [34], Zhang et al. [32], Si et al. [33] and Wu et al. [9]; D =volume-based D_{90} in Yao et al. [35].

the [Supplementary Material](#). It shows that the data in this work agrees well with Xiang et al. [34]. However, there is a large deviation in different work even at the same gap height, especially the numerical work, in which smooth base was sometimes used. For example, in the work of Wu et al. [9], spherical Mo particles ($D_{50} = 36 \mu\text{m}$, $\Gamma = 0.0597 \text{ mJ/m}^2$) and smooth plate were used, resulting in very low value of total particle volume of spread layer, which is due to the mechanism shown above. It suggests that the frictional behaviour between particles and base is important to obtain a good agreement between the simulation and experiment. Based on the data shown in Fig. 19, the largest normalised particle volume of spread layer at each gap height could be

predicted, given as:

$$\phi_{\max} = \phi_{\max 0} \left[1 - \frac{1}{\exp(ax)} - \frac{1}{\exp(bx)} \right] \quad (11)$$

where $x = \delta/D$ is the normalised gap height; $\phi_{\max 0} = 0.47$ is the largest normalised particle volume of spread layer; $a = 0.38$ is the parameter describing blade shearing action and base stagnation effect on the heap, as well as particle jamming around the gap, while $b = 2.85$ is the constant describing the effect of powder flowability on the movement of particles within the heap. Based on Eq. (11), the maximum fraction of spread layer at the specified gap height in the AM machine could be predicted, which provides a reference when tuning operation conditions, such as changing materials (including PSD and shape) and spreading speed.

6. Conclusions

In this study, the spreadability of powder used in powder-based additive manufacturing is detailed investigated. The metrics of spreadability are examined for powder with different size classes, and the factors affecting powder spreadability are analysed, including the cohesion number and rolling friction of particles. The simulation results are also validated by comparing the total particle volume of spread layer against the experimental and numerical data in previous work. The main results from the present study are summarised as follows:

- 1) Three kinds of metrics are proposed to quantify powder spreadability. Relative powder spreadability should be compared at the same ratio of the gap height to particle size, especially for powders with different particle size classes. Powder spreadability is not directly related to powder flowability, although the spreadability of the powder with good flowability is usually not bad.
- 2) Powder spreadability is mainly controlled by the shear action of the blade on the heap, the stagnation effect due to the rough surface of base, and particle jamming around the gap region, and the effect of powder flowability on the movement of particles within the heap. A physical model is proposed to predict the maximum fraction of spread layer at the specified gap height that could be realised by tuning operation conditions.
- 3) With the increase of cohesion number of particles, the shear strength of the blade on the heap is reduced, resulting in the decrease of spreadability. For the case with large cohesion number, particles tend to form agglomerates, and the heap even does not contact well with the spreader. With the increase of rolling friction of particles, the interlocking between particles not only suspends the re-filling process of particles within the heap, but also promotes particle jamming around the gap, resulting in a significant decrease of spreadability.
- 4) As a result of particle jamming, powder spreadability is more sensitive to the rolling friction or particle interlocking than particle cohesion for the cases considered in this work, although the rheological behaviour is similar in front of the gap. The spreadability is also sensitive to the frictional behaviour between the heap and the base. For the base without enough roughness, the particles with large rolling friction could even not be spread, in which particle jamming could be observed for a long time.

CRediT authorship contribution statement

Rui Xu: Writing – original draft, Investigation. **Wenguang Nan:** Writing – review & editing, Investigation, Conceptualization.

Declaration of Competing Interest

The authors declare that they have no known competing financial

interests or personal relationships that could have appeared to influence the work reported in this paper.

Data Availability

Data will be made available on request.

Appendix

The stress tensor of the particle flow within the cell is given as:

$$\sigma_{ij} = \frac{1}{V} \left(\sum_{p \in V} m_p \delta v_i \delta v_j + \sum_{c \in V} f_{ij} \cdot r_{ij} \right) \quad (1)$$

where V is the volume of the cell; m_p is the mass of particle p ; δv_i and δv_j are the fluctuation velocities of particle p ; f_{ij} is the contact force at contact c and r_{ij} is the corresponding branch vector between mass centre of particle i and that of particle j . Based on the stress tensor, three principal stresses could be calculated: major one σ_1 , intermediate one σ_2 and minor one σ_3 . The normal stress σ and shear stress τ are then given as:

$$\sigma = \frac{\sigma_1 + \sigma_2 + \sigma_3}{3} \quad (2)$$

$$\tau = \frac{\sqrt{(\sigma_1 - \sigma_2)^2 + (\sigma_1 - \sigma_3)^2 + (\sigma_2 - \sigma_3)^2}}{\sqrt{6}} \quad (3)$$

The bulk friction μ_b is calculated as the ratio of shear stress to normal stress. Similar to the rheological analysis of dense particle flow [36], inertial number I is used to normalise shear rate:

$$I = \gamma D_{90} \sqrt{\rho_p / \sigma} \quad (4)$$

where γ is the shear strain rate, which is simplified as $\gamma = U/\delta$ in this work.

Appendix A. Supporting information

Excel worksheet is provided for the raw information involved in the data used for comparison of total particle volume of spread layer, which can be found in the online version at [doi:10.1016/j.addma.2023.103596](https://doi.org/10.1016/j.addma.2023.103596).

References

- [1] T.D. Ngo, A. Kashani, G. Imbalzano, K.T.Q. Nguyen, D. Hui, Additive manufacturing (3D printing): a review of materials, Methods, Appl. Chall., Compos. Part B: Eng. 143 (2018) 172–196.
- [2] W.E. Frazier, Metal additive manufacturing: a review, J. Mater. Eng. Perform. 23 (6) (2014) 1917–1928.
- [3] N. Guo, M.C. Leu, Additive manufacturing: technology, applications and research needs, Front. Mech. Eng. 8 (3) (2013) 215–243.
- [4] D.D. Gu, W. Meiners, K. Wissenbach, R. Poprawe, Laser additive manufacturing of metallic components: materials, processes and mechanisms, Int. Mater. Rev. 57 (3) (2013) 133–164.
- [5] D. Oropesa, R.W. Penny, D. Gilbert, A.J. Hart, Mechanized spreading of ceramic powder layers for additive manufacturing characterized by transmission x-ray imaging: Influence of powder feedstock and spreading parameters on powder layer density, Powder Technology (2021).
- [6] S. Yim, H. Bian, K. Aoyagi, K. Yamanaka, A. Chiba, Spreading behavior of Ti 48Al 2Cr 2Nb powders in powder bed fusion additive manufacturing process: Experimental and discrete element method study, Addit. Manuf. (2021).
- [7] H. Chen, Y. Chen, Y. Liu, Q. Wei, Y. Shi, W. Yan, Packing quality of powder layer during counter-rolling-type powder spreading process in additive manufacturing, Int. J. Mach. Tools Manuf. 153 (2020).
- [8] L. Cordova, T. Bor, M. de Smit, M. Campos, T. Tinga, Measuring the spreadability of pre-treated and moisturized powders for laser powder bed fusion, Addit. Manuf. 32 (2020).
- [9] Y. Wu, M. Li, J. Wang, Y. Wang, X. An, H. Fu, H. Zhang, X. Yang, Q. Zou, Powder-bed-fusion additive manufacturing of molybdenum: process simulation, optimization, and property prediction, Addit. Manuf. 58 (2022).
- [10] Y. He, A. Hassanpour, A.E. Bayly, Combined effect of particle size and surface cohesiveness on powder spreadability for additive manufacturing, Powder Technol. 392 (2021) 191–203.
- [11] D. Schiochet Nasato, H. Briesen, T. Pöschel, Influence of vibrating recoating mechanism for the deposition of powders in additive manufacturing: Discrete element simulations of polyamide 12, Addit. Manuf. 48 (2021).
- [12] D.Z. Yao, X.Z. An, H.T. Fu, H. Zhang, X.H. Yang, Q.C. Zou, K.J. Dong, Dynamic investigation on the powder spreading during selective laser melting additive manufacturing, Addit. Manuf. 37 (2021) 12.
- [13] Y. Zhao, J.W. Chew, Effect of lognormal particle size distributions on particle spreading in additive manufacturing, Adv. Powder Technol. 32 (4) (2021) 1127–1144.
- [14] J. Zhang, Y. Tan, T. Bao, Y. Xu, X. Xiao, S. Jiang, Discrete element simulation of the effect of roller-spreading parameters on powder-bed density in additive manufacturing, Mater. (Basel) 13 (10) (2020).
- [15] H. Chen, Q. Wei, Y. Zhang, F. Chen, Y. Shi, W. Yan, Powder-spreading mechanisms in powder-bed-based additive manufacturing: Experiments and computational modeling, Acta Mater. 179 (2019) 158–171.
- [16] S. Haeri, Y. Wang, O. Ghita, J. Sun, Discrete element simulation and experimental study of powder spreading process in additive manufacturing, Powder Technol. 306 (2017) 45–54.
- [17] M.H. Sehhat, A. Mahdiankhotbesara, Powder spreading in laser-powder bed fusion process, Granul. Matter 23 (4) (2021).
- [18] W. Nan, M. Pasha, T. Bonakdar, A. Lopez, U. Zafar, S. Nadimi, M. Ghadiri, Jamming during particle spreading in additive manufacturing, Powder Technol. 338 (2018) 253–262.
- [19] M. Ghadiri, M. Pasha, W. Nan, C. Hare, V. Vivacqua, U. Zafar, S. Nezamabadi, A. Lopez, M. Pasha, S. Nadimi, Cohesive powder flow: trends and challenges in characterisation and analysis, KONA powder and particle, Journal 37 (0) (2020) 3–18.
- [20] Z. Snow, R. Martukanitz, S. Joshi, On the development of powder spreadability metrics and feedstock requirements for powder bed fusion additive manufacturing, Addit. Manuf. 28 (2019) 78–86.
- [21] M. Ahmed, M. Pasha, W. Nan, M. Ghadiri, A simple method for assessing powder spreadability for additive manufacturing, Powder Technol. 367 (2020) 671–679.
- [22] T.-P. Le, X. Wang, K.P. Davidson, J.E. Fronda, M. Seita, Experimental analysis of powder layer quality as a function of feedstock and recoating strategies, Addit. Manuf. 39 (2021).
- [23] A. Mussatto, R. Groarke, A. O'Neill, M.A. Obeidi, Y. Delaure, D. Brabazon, Influences of powder morphology and spreading parameters on the powder bed

- topography uniformity in powder bed fusion metal additive manufacturing, *Addit. Manuf.* 38 (2021).
- [24] W. Nan, Y. Gu, Experimental investigation on the spreadability of cohesive and frictional powder, *Adv. Powder Technol.* 33 (3) (2022).
- [25] M.Y. Shaheen, A.R. Thornton, S. Luding, T. Weinhart, The influence of material and process parameters on powder spreading in additive manufacturing, *Powder Technol.* 383 (2021) 564–583.
- [26] W. Nan, M. Pasha, M. Ghadiri, Effect of gas-particle interaction on roller spreading process in additive manufacturing, *Powder Technol.* 372 (2020) 466–476.
- [27] C. Thornton, *Granular Dynamics. Contact Mechanics and Particle System Simulations*, Springer, New York, 2015.
- [28] P.A. Cundall, O.D.L. Strack, A discrete numerical model for granular assemblies, *Geotechnique* 29 (1979) 47–65.
- [29] K.L. Johnson, K. Kendall, A.D. Roberts, Surface energy and the contact of elastic solids, *Proc. R. Soc. Lond. A. Math. Phys. Sci.* 324 (1971) 301–313.
- [30] W. Nan, M. Ghadiri, Numerical simulation of powder flow during spreading in additive manufacturing, *Powder Technol.* 342 (2019) 801–807.
- [31] W. Nan, M. Pasha, M. Ghadiri, Numerical simulation of particle flow and segregation during roller spreading process in additive manufacturing, *Powder Technol.* 364 (2020) 811–821.
- [32] J. Zhang, Y. Tan, X. Xiao, S. Jiang, Comparison of roller-spreading and blade-spreading processes in powder-bed additive manufacturing by DEM simulations, *Particuology* 66 (2022) 48–58.
- [33] L. Si, T. Zhang, M. Zhou, M. Li, Y. Zhang, H. Zhou, Numerical simulation of the flow behavior and powder spreading mechanism in powder bed-based additive manufacturing, *Powder Technol.* 394 (2021) 1004–1016.
- [34] Z. Xiang, M. Zhang, R. Yan, Q. Yin, K. Zhang, Powder-spreading dynamics and packing quality improvement for laser powder bed fusion additive manufacturing, *Powder Technol.* 389 (2021) 278–291.
- [35] D. Yao, X. Liu, J. Wang, W. Fan, M. Li, H. Fu, H. Zhang, X. Yang, Q. Zou, X. An, Numerical insights on the spreading of practical 316 L stainless steel powder in SLM additive manufacturing, *Powder Technol.* 390 (2021) 197–208.
- [36] W. Nan, M. Ghadiri, Y. Wang, Analysis of powder rheometry of FT4: effect of air flow, *Chem. Eng. Sci.* 162 (2017) 141–151.